Exponential error reduction for glueball calculations using a two-level algorithm in pure gauge theory

Lorenzo Barca[*] and Stefan Schaefer[†]

John von Neumann-Institut für Computing NIC, Deutsches Elektronen-Synchrotron DESY, Platanenallee 6, 15738 Zeuthen, Germany

Francesco Knechtli[‡] and Juan Andrés Urrea-Niño[§]

Department of Physics, University of Wuppertal, Gaußstrasse 20, 42119 Germany

Sofie Martins[‖]

ħQTC & IMADA, University of Southern Denmark, Campusvej 55, 5230 Odense M, Denmark

Michael Peardon[¶]

School of Mathematics, Trinity College Dublin, 2 Dublin, Ireland

(Received 19 June 2024; accepted 3 September 2024; published 23 September 2024)

This study explores the application of a two-level algorithm to enhance the signal-to-noise ratio of glueball calculations in four-dimensional SU(3) pure gauge theory. Our findings demonstrate that the statistical errors exhibit an exponential reduction, enabling reliable extraction of effective masses at distances where current standard methods would demand exponentially more samples. However, at shorter distances, standard methods prove more efficient due to a saturation of the variance reduction using the multilevel method. We discuss the physical distance at which the multilevel sampling is expected to outperform the standard algorithm, supported by numerical evidence across different lattice spacings and glueball channels. Additionally, we construct a variational basis comprising 35 Wilson loops up to length 12 and 5 smearing sizes each, presenting results for the first state in the spectrum for the scalar, pseudoscalar, and tensor channels.

DOI: 10.1103/PhysRevD.110.054515

I. INTRODUCTION

One consequence of confinement of quarks and gluons by the strong force in quantum chromodynamics (QCD) is the possible existence of glueballs [1,2], states predominantly made of gluons. These hypothetical composites have been studied widely within a range of theoretical frameworks, such as the bag model [3–6], flux-tube model [7,8] and QCD sum rules [9–12] and have been investigated from first principles since the development of lattice QCD methods [13–17]. Finding experimental evidence for glueballs remains a challenge [18] as the lightest candidates suggested by theoretical studies are rather massive, approaching twice the mass of a nucleon and have quantum numbers in common with some quark-model mesons. As a result, physical states at this energy scale are mixtures of conventional isoscalar mesons and glueballs and have large phase-space for decay to multiple light mesons [19–23]. Very little is known about the decay processes of the glueball in QCD, so reliable interpretation of resonances in collider experiments as glueballs is challenging. There have been a number of experimental observations of candidates [24], mostly identified as an overpopulation of resonances compared to quark model predictions, but their link to QCD remains unresolved. Recent experimental confirmation of pseudoscalar quantum numbers for the X(2370) [25] have given fresh incentive to these studies.

Lattice QCD calculations can provide a great deal of information to guide these searches from first principles. Ideally, the spectrum is computed on the lattice, including the dynamics of the quark and gluon fields [26–32] which causes both mixing of quark-model mesons with the glueballs and their strong decays. Then, widths of the

[*]Contact author: lorenzo.barca@desy.de
[†]Contact author: stefan.schaefer@desy.de
[‡]Contact author: knechtli@uni-wuppertal.de
[§]Contact author: urreanino@uni-wuppertal.de
[‖]Contact author: martinss@imada.sdu.dk
[¶]Contact author: mjp@maths.tcd.ie

resulting resonances can be studied following ideas introduced by Luscher [33] which relate the energy spectrum in a finite volume to certain scattering phase shifts. Developing this framework beyond two-body elastic scattering is a very active research topic [34], but the input which lattice calculations must provide remains the accurate determination of a complete low-energy spectrum of QCD in a finite volume. This can only be computed in practice by determining two-point correlation functions between a broad range of creation and annihilation operators resembling glueballs, quark-model isoscalar mesons, two-pion states, and so on.

One difficulty with these calculations arises from use of importance-sampling Monte Carlo estimates. The spectrum is extracted from the Euclidean-time dependence of correlation functions, which fall exponentially with a rate governed by the energies of the states under investigation. In glueball calculations, the relevant scale is typically beyond 1.5 GeV. The Monte Carlo estimators have high statistical variance, roughly independent of the Euclidean time separation. As a result, the signal-to-noise ratio falls rapidly [35,36] and very large statistical ensembles, typically with $\mathcal{O}(10^5)$ samples, are needed for high precision.

This study tests and models the behavior of improved Monte Carlo methods offering better signal-to-noise performance. Our investigation is restricted to the pure Yang-Mills SU(3) theory; there is active research [37–41] into extensions of these techniques to QCD, including the dynamics of the quark fields outside the scope of this paper. Calculations with fermions present significant technical challenges due to the glueball-meson mixing and the nonlocality of the quark propagators and fermion determinants. Locality of the Yang-Mills action along with bosonic statistics of gluons allows factorization of the observables of the lattice field theory into subvolume integrals, which can be sampled independently by drawing random field variables from the appropriate conditional distributions and constructing full observables with smaller variance from products of these independent samples. The first use of this factorization was the *multihit algorithm* [42], introduced in computations of the string tension. The algorithm was subsequently extended to *multilevel* methods [43], achieving exponential error reduction for certain observables. Later work [44–47] investigated these schemes for glueball calculations where the temporal extent of the lattice is divided into nested subdomains and expectation values estimated by hierarchical Markov chain Monte Carlo calculations inside these layers.

The paper extends earlier work [48] testing these schemes in detail and is organized as follows. Section II reviews the multilevel sampling algorithm, focussing on determinations of glueball correlation functions. Section III presents the findings of our calculation, including detailed analysis of the performance of the method when using a large basis of operators suitable for spectrum calculations based on solving a generalized eigenvalue problem (GEVP) [49–51]. These techniques are the key to reliable studies when mixing with quarkonia or decays into multiple hadrons are investigated. Comparisons with state-of-the-art calculations are made, and statistical precision is studied in detail. Our conclusions are presented in Sec. IV.

II. THE MULTILEVEL SAMPLING ALGORITHM

Energy eigenstates can be investigated using two-point correlation functions of quantum fields on an Euclidean lattice. Their efficient determination in Monte Carlo calculation using a multilevel algorithm proceeds as follows.

A. Algorithmic details

The correlation function of two operators $\mathrm{O}(t_1)$ and $\bar{\mathrm{O}}(t_0)$ is defined as

$$C(t_1,t_0) \equiv \langle \mathrm{O}(t_1)\bar{\mathrm{O}}(t_0)\rangle = \frac{1}{\mathcal{Z}}\int dU\, e^{-S(U)}\mathrm{O}(U,t_1)\bar{\mathrm{O}}(U,t_0), \quad (1)$$

where $\mathcal{Z}$ is the partition function, and S is the Euclidean action. This integral can be estimated numerically with Monte Carlo techniques, by generating an ensemble of N gauge configurations $\{U_1, U_2, \ldots U_N\}$, drawn from a sample distribution with probability $P(U_i) \propto e^{-S(U_i)}$. We then estimate the correlation by computing

$$\hat{C}(t_1,t_0)_{\text{standard}} = \frac{1}{N}\sum_{i=1}^{N}\mathrm{O}(U_i,t_1)\bar{\mathrm{O}}(U_i,t_0) \quad (2)$$

with the associated standard error

$$\sigma_C(t_1,t_0;N) = \sqrt{\frac{\mathrm{var}(\mathrm{O}(t_1)\bar{\mathrm{O}}(t_0))}{N}}, \quad (3)$$

which depends on the decorrelated sample size N and variance

$$\mathrm{var}(\mathrm{O}(t_1)\bar{\mathrm{O}}(t_0)) = \langle(\mathrm{O}(t_1)\bar{\mathrm{O}}(t_0))^2\rangle - \langle \mathrm{O}(t_1)\bar{\mathrm{O}}(t_0)\rangle^2. \quad (4)$$

Multi-level simulations, [42–44] were introduced after observing the path integral of the correlation function in a pure gauge theory factorizes into subdomains

$$C(t_1,t_0) = \int dU_B \Bigg\{ \frac{e^{-S_B(U_B)}\mathcal{Z}_1(U_B)\mathcal{Z}_2(U_B)}{\mathcal{Z}} \times \int dU^{(1)} \frac{e^{-S_1(U^{(1)}|U_B)}}{\mathcal{Z}_1(U_B)} \mathrm{O}(U^{(1)},t_1) \times \int dU^{(2)} \frac{e^{-S_2(U^{(2)}|U_B)}}{\mathcal{Z}_2(U_B)} \bar{\mathrm{O}}(U^{(2)},t_0) \Bigg\} = \langle [\mathrm{O}(U^{(1)},t_1)][\bar{\mathrm{O}}(U^{(2)},t_0)] \rangle, \quad (5)$$

where we are using, in addition to the established expectation $\langle \ldots \rangle$, the subaverage as defined in [43]

$$[\mathrm{O}(U^{(r)},t)] = \int dU^{(r)} \frac{e^{-S_r(U^{(r)}|U_B)}}{\mathcal{Z}_r(U_B)} \mathrm{O}(U^{(r)},t), \quad (6)$$

with

$$\mathcal{Z}_r(U_B) = \int dU^{(r)} e^{-S_r(U^{(r)}|U_B)}. \quad (7)$$

Here, we denote U_B as gauge fields on fixed boundaries, while $U^{(1)}$ and $U^{(2)}$ are gauge fields whose dynamics are determined by the conditional actions S_1 and S_2. The superscripts of $U^{(1)}$ and $U^{(2)}$ refer to the two different regions.

This decomposition splits the lattice into two independent domains depending on the fixed boundary B separating them. The path integrals on the subdomains can then be approximated by simulating only the subdomain with fixed boundary conditions. In practice, we initially generate a regular Monte Carlo chain of N_0 configurations, denoted as U_i for $i = 1, \ldots, N_0$. These are referred to as *level-0* configurations. The fields restricted to B are subsequently distributed according to the marginal probability density in the U_B integration in Eq. (5).

From each of these level-0 configurations, we generate a subchain of configurations updated in each sweep only on partial domains but left unchanged on the remaining temporal domains. These subchains are generated with fixed boundary conditions, drawn from the conditional probability density in the $U^{(r)}$-integrals in Eq. (5). We refer to the updated domains as the *dynamical regions*, while the other time slices are the *fixed regions*, which separate two different dynamical ones. We use the notation Λ_k to refer to the specific sublattice decomposition in dynamical and frozen regions of the subchains. In Fig. 1, there is one example of sublattice decompositions adopted in this work. The blue-shaded regions at $t = 11a, 23a, \ldots (35a, 47a)$ are the fixed regions, consisting of only one time slice each, and the other time slices are the dynamical regions, where the fields U_i are updated along the level-1 chain. The temporal gauge links connecting the fixed with the dynamical regions are updated. We label these *level-1* configurations, U_{ij} using a second index $j \in 1, \ldots, N_1$ to indicate the trajectory time along the subchains, while i indicates the initial level-0 configuration. Thus we generate $N_0 \times N_1$ gauge configurations, labeled U_{ij}. Using the Wilson plaquette action, fixed regions comprised of a single time slice are sufficient to separate the dynamical regions such that gauge updates are independent, whereas for improved gauge actions which include larger Wilson loops such as the Lüscher-Weisz, the width of the frozen regions must be increased [52].

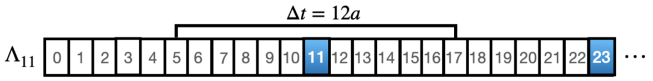

FIG. 1. Example of the sublattice decomposition Λ_{11} (ellipses represent $t/a \geq 24$), where the dynamical regions are eleven lattice spacings wide. The angled connecting line visualizes the correlation between operators measured in two different dynamical regions. For instance, in this case, one at $t_0 = 5a$ and the other operator at $t_1 = t_0 + \Delta t = 17a$.

When the operators are in two different dynamical regions, the multilevel estimator reads

$$\hat{C}(t_1,t_0) = \frac{1}{N_0}\sum_{i=1}^{N_0}\left(\frac{1}{N_1}\sum_{j=1}^{N_1}\mathrm{O}_{ij}(t_1)\right)\left(\frac{1}{N_1}\sum_{k=1}^{N_1}\bar{\mathrm{O}}_{ik}(t_0)\right) \quad \text{for } t_0, t_1 \text{ in different domains}, \quad (8)$$

which corresponds to a combination of two independent level-1 averages followed by a level-0 average. We will confirm that this reduces noise sufficiently to make it equivalent to a standard measurement with $N_0 \times N_1^2$ samples up to boundary corrections. Then the error scales ideally like $\sigma_C(t_1,t_0;N_0;N_1) \sim 1/\sqrt{N_0 N_1^2}$, as one can guess from the scaling of this estimator with N_0 and N_1. Corrections to this ideal scaling are discussed in the following subsection. The factorization in Eq. (5) applies only when the operators are in two different regions.

When the operators are in the same region, and therefore when t_0 and t_1 belong to the same domain, the level-1 and level-0 measurements give a unique sample, and we have to employ the standard estimator

$$\hat{C}(t_1,t_0) = \frac{1}{N_0 N_1}\sum_{i=1}^{N_0}\sum_{j=1}^{N_1}\mathrm{O}_{ij}(t_1)\bar{\mathrm{O}}_{ij}(t_0) \quad \text{for } t_0, t_1 \text{ in same domain}, \quad (9)$$

where at best the error scales like $\sigma_C(t_1,t_0;N_0;N_1) \sim 1/\sqrt{N_0 N_1}$ as in Eq. (3).

B. The noise-to-signal ratio

The spectral decomposition of the correlation functions, estimated with Monte Carlo algorithms, exhibits an exponential decay of the signal over time as

$$C(t_1,t_0) = \langle \mathrm{O}(t_1)\bar{\mathrm{O}}(t_0)\rangle = \sum_n |\langle 0|\mathrm{O}(0)|n\rangle|^2 e^{-E_n(t_1-t_0)} \overset{t_1\gg t_0}{\sim} e^{-m(t_1-t_0)}, \tag{10}$$

with E_n, the energy of a state with the quantum numbers of the zero-momentum operator O, and m, the ground-state mass. Since in our investigation $\mathrm{O}(t)$ is a glueball operator, m is the mass of the ground-state glueball.

The variance of a glueball correlation function computed with traditional algorithms is approximately constant [35,36] as the source-sink separation $t_1 - t_0$ varies. Thus, its noise-to-signal ratio increases exponentially as

$$\frac{\sigma_C(t_1,t_0;N)}{C(t_1,t_0)} \sim \frac{1}{\sqrt{N}} e^{m(t_1-t_0)}, \tag{11}$$

and to keep the relative precision constant at all time separations, one must record $N \sim e^{2m(t_1-t_0)}$ measurements. However, if the correlation function is estimated with multilevel algorithms using Eq. (8), the noise-to-signal ratio becomes

$$\frac{\sigma_C(t_1,t_0;N_0;N_1)}{C(t_1,t_0)} \sim \frac{1}{\sqrt{N_0 N_1^2}} e^{m(t_1-t_0)}, \tag{12}$$

where clearly, performing the additional N_1 submeasurements keeps the relative error fixed much more efficiently. Indeed, performing $N_1 \approx e^{m(t_1-t_0)}$ more submeasurements for each operator O keeps the error fixed, as opposed to $N \approx e^{2m(t_1-t_0)}$ with the traditional algorithm. There is a clear exponential improvement.

However, the expression in Eq. (12) is correct up to fluctuations arising from the boundaries, i.e., the fixed regions, but $N_1 \approx e^{m(t_1-t_0)}$ will still be enough to keep the relative error constant, as we discuss below. In general, by taking into account fluctuations from the fixed boundaries, one can derive the expression for the variance of the multilevel correlation function [53], which reads

$$\sigma_C^2(t_1,t_0;N_0;N_1) \approx \frac{c_0^2}{N_0 N_1^2} + \frac{c_1^2}{N_0 N_1}\left(e^{-\tilde{m}\Delta_1} + e^{-\tilde{m}\Delta_0}\right) + \frac{c_2^2}{N_0} e^{-\tilde{m}(\Delta_1+\Delta_0)}, \tag{13}$$

with c_0, c_1, c_2 of similar order of magnitude. In this formula, Δ_1 and Δ_0 denote the distance of the operators at t_1 or t_0 respectively to the nearest boundaries at t_B.

Equation (13) contains important information on the dependence of multilevel algorithm performance on the parameter choice. The time-independent term of the multilevel error $\sigma_C(t_1,t_0;N_0,N_1)$ scales with $1/\sqrt{N_0 N_1^2}$, up to exponential fluctuations induced by the fixed boundaries. The multilevel error decreases with the number of submeasurements N_1 until the last term in Eq. (13), which is independent of N_1, becomes relevant. Note the formula in Eq. (13) accounts only for fluctuations from one nearest boundary for each operator, while in general, one has to consider all the boundary fluctuations.

We must emphasize an important caveat: Numerically, we find that the mass in the exponent of the boundary fluctuations corresponds to twice the mass of a glueball state, $\tilde{m} = 2m^\Gamma$, in that particular glueball channel $\Gamma \equiv R^{PC}$, which identifies a specific lattice irreducible representation R of the group of rotations of the cube with parity P and charge conjugation C. In all glueball channels, we expect states with vacuum quantum numbers to contribute at long distances and to be suppressed at short distances due to small overlap. Unfortunately, we do not have sufficient data to show this.

C. Saturation of the variance reduction

The multilevel error reduction is explicitly dependent on the level-1 submeasurements and the distance of the operators from the nearest boundaries. In particular, there is a critical number of submeasurements $\tilde{N}_1$, above which the multilevel error does not reduce further with N_1. This saturation point is reached when the first two terms in Eq. (13) become the same order of magnitude as the last.

As a result, for operators symmetrically distant from the boundaries, i.e., $\Delta_1 = \Delta_0 = \Delta t/2$, with $\Delta t = t_1 - t_0$ and $N_1 \gg \tilde{N}_1 \sim \exp(m^\Gamma \Delta t)$, the multilevel error decreases exponentially like $\sim\exp(-m^\Gamma \Delta t)$ and consequently the relative error stays constant with increasing Δt. As noted in Sec. II B, we see here again the origin of the noise reduction: For the standard Monte Carlo method, we need to rescale the number of measurements with $\sim\exp(2m^\Gamma \Delta t)$ while now we need only $\sim\exp(m^\Gamma \Delta t)$ more measurements in a multilevel simulation to achieve a constant relative error.

However, at short distance, this represents a limitation compared to the traditional error scaling. While the multilevel error is independent of N_1 for $N_1 \gg \tilde{N}_1$, the traditional scaling decreases as $1/\sqrt{N_1}$, modulo exponential fluctuations from the boundaries. Therefore, at short distance, it is better to measure the correlations between operators located in the same dynamical regions, whose error scales like the traditional scaling. There is an intermediate distance $\Delta\tilde{t}$ where the saturated multilevel starts to outperform the standard scaling. This occurs when

$$\exp\left(-m^\Gamma \Delta\tilde{t}\right) \lesssim \frac{1}{\sqrt{N_1}} \tag{14}$$

is satisfied, assuming that the coefficients c_i in Eq. (13) are of the same order. Our simulations confirm this behavior, as shown in the next section. For instance, on the ensemble *gb62*, it is clear from Figs. 3,4 that the transition point for the E^{++} channel with $am^{E^{++}} \approx 0.77$ and $N_1 = 1000$ is between $4a \leq \Delta\tilde{t} \leq 6a$.

The variance of the correlation function $C(t_1, t_0)$ is clearly not the same for each t_0, even at fixed Δt. To take advantage of all the measurements for a given distance $\Delta t = t_1 - t_0$, we consider the weighted average

$$\bar{C}(\Delta t) = \frac{\sum_{t_0} w(t_0 + \Delta t, t_0) C(t_0 + \Delta t, t_0)}{\sum_{t_0} w(t_0 + \Delta t, t_0)}, \quad (15)$$

where we choose the weights $w(t_1, t_0) = 1/\sigma_C^2 \times (t_1, t_0; N_0; N_1)$. This weighted average selects the best correlation from either the standard correlation of operators in the same domain for short distances or multilevel correlations of operators separated equally from a fixed boundary in different domains for long distances. There is more discussion on optimum weighting for multilevel algorithms in [54].

Due to the weighted average, there is a transition between different error scalings: At sufficiently long distance $\Delta t = t_1 - t_0 \gtrsim \Delta\tilde{t}$, which depends on the glueball channel, cf. Eq. (14), from Eq. (13) we expect the variance-to-signal ratio of the weighted average in Eq. (15) for a specific glueball channel Γ to be

$$\frac{\sigma_{\bar{C}}^2(\Delta t)}{\bar{C}^2(\Delta t)} \approx \frac{\tilde{c}_0^2}{N_0 N_1^2} e^{2m^\Gamma \Delta t} + \frac{2\tilde{c}_1^2}{N_0 N_1} e^{2m^\Gamma \Delta t/2} + \frac{\tilde{c}_2^2}{N_0} \quad \text{for } \Delta t \gtrsim \Delta\tilde{t}, \quad (16)$$

where the term increasing exponentially with Δt is divided by N_1^2 rather than N_1, thus rendering a substantial improvement at large distance. At short distance, the noise-to-signal ratio of the weighted average is expected to scale like

$$\frac{\sigma_{\bar{C}}^2(\Delta t)}{\bar{C}^2(\Delta t)} \approx \frac{\tilde{a}_0^2}{N_0 N_1} e^{2m^\Gamma \Delta t} \quad \text{for } \Delta t \lesssim \Delta\tilde{t}, \quad (17)$$

where $\tilde{a}_0^2 \propto \mathrm{var}(\mathrm{O}(\Delta t)\bar{\mathrm{O}}(0a))$, cf. Eq. (3). Thus, the weighted average exhibits two different scalings at short and long distances, and the transition between the two behaviors occurs when Eq. (14) is fulfilled.

III. SIMULATIONS

The performance of the multilevel method was examined in several numerical computations of a lattice discretization of $4D$ SU(3) Yang-Mills theory as described in this section.

TABLE I. Overview of ensembles. The tag *Level-1 decomposition* denotes the size of the fixed and dynamical regions in the format: *width of fixed region + width of dynamical region*. The lattice sizes and dynamical regions are scaled to have the same physical size. Simulations are performed using the HMC with $\tau = 3.0$, where the level-0 configurations are separated by 300 MDUs (molecular dynamics units). All ensembles consist of $N_0 = 101$ level-0 and $N_1 = 1000$ level-1 configurations. The scale setting is made through the Sommer scale $r_0 = 0.5$ fm according to [57].

Name	T/a	L/a	Level-1 decomposition	β	a fm
gb62	48	24	$\Lambda_{11} = 1 + 11$	6.2	0.068
gb608	40	20	$\Lambda_9 = 1 + 9$	6.08	0.081
gb58	24	12	$\Lambda_5 = 1 + 5$	5.8	0.136

A. Details

We simulate the Wilson pure gauge action

$$S_g = \frac{\beta}{3} \sum_{n \in \Lambda} \sum_{\mu < \nu} \mathrm{Re}\{\mathrm{Tr}[1 - U_\mu(n) U_\nu(n + \hat{\mu}) \times U_\mu^\dagger(n + \hat{\nu}) U_\nu^\dagger(n)]\} \quad (18)$$

with periodic boundary conditions, and we investigate $\beta = 5.8$, 6.08, 6.2 with a physical volume kept roughly constant to $V = T \times L^3 = (3.26\ \mathrm{fm}) \times (1.63\ \mathrm{fm})^3$ using a modified version of OpenQCD [55,56]. See Table I for an overview of the ensembles analyzed in this work. For each β, we generate $N_0 = 101$ gauge configurations with the traditional HMC algorithm, i.e., the gauge configurations are updated on the entire volume. We choose well spaced configurations such that the autocorrelations are negligible. For each of these level-0 configurations, a new, independent Monte Carlo chain is generated using HMC, as discussed in Sec. II A. In particular, on the ensemble *gb62* at $\beta = 6.2$, with $L = 24a$, $T = 48a$, the level-1 gauge configurations are kept fixed on time slices $t = 11a$, $23a, 35a, 47a$, while updated everywhere else. This way, there are four regions where the gauge fields are updated independently. This decomposition is labeled Λ_{11} since the dynamical regions comprise 11 lattice sites, corresponding to ~0.75 fm each, as seen in Fig. 1. Since we are interested in the glueball spectrum, the observable $\mathrm{O}(t)$ is a glueball operator, which in pure gauge theory can be constructed from Wilson loops. Appendix gives more detail on constructing glueball operators projected onto a specific lattice irreducible representation R^{PC}. This work investigates $\Gamma \equiv R^{PC} = A_1^{++}, E^{++}, T_2^{++}$, and A_1^{-+}. For each operator O^Γ we estimate the correlation function $C^\Gamma(t_1, t_0)$ using Eq. (8) when the operators are in two different regions, while when the operators are in the same region, we estimate the correlation function using Eq. (9). When the two operators are in different dynamical regions, the error

should scale according to Eq. (13). However, if the operators are in the same region, the error is almost constant over time and should scale like $1/\sqrt{N_1}$, see Eq. (3).

B. Analysis of the statistical precision

Figure 2 shows the standard error of the correlation function $C^\Gamma(t_1, t_0)$ for $\Gamma = E^{++}$ at $t_0 = 5a$ (top), and $t_0 = 9a$ (bottom) for different values of t_1. The source operator is fixed at t_0 while the sink operator at t_1 is moved to determine the dependence of the error on the distance of the sink from the boundaries. The correlation function is computed on the ensemble *gb62* using the level-1 decomposition Λ_{11}, see Fig. 1. When the two operators are measured in different regions, the statistical uncertainty follows a $\cosh$ behavior as the operator moves between adjacent boundaries. As the large N_1 limit is approached, the error decreases exponentially according to $\exp(-m^\Gamma \Delta_1)\exp(-m^\Gamma \Delta_0)$ when $11 \leq t_1/a \leq 23$. In contrast, when the operators are in the same dynamical region $(0 \leq t_1/a \leq 10)$, statistical fluctuations are independent of separation, so the uncertainty falls only in inverse proportion to $\sqrt{N_1}$. Using a global fit to the data using Eq. (13), we find $c_0 \approx c_1, c_2$. This model behavior is compared to our data on the figure along with the limiting behavior when $N_1 \to \infty$. In this limit, the third term in the expression, independent of N_1, persists, which suggests subsampling more than $N_1 \propto e^{m^\Gamma \Delta t}$ measurements does not improve precision any further.

The four panels of Fig. 3 show the dependence of the error on the operator location relative to the boundaries for different values of N_1, for $\Delta t/a = 2$, 4, 6 and 12. As before, for certain values of t_0, the two operators are in the same sampling region, so the error is proportional to $1/\sqrt{N_1}$. In contrast, for values of t_0 where the operators are in different regions, the error behaves according to Eq. (13). The x-axis is chosen so operators symmetrically distant from the boundaries are horizontally aligned, emphasizing the error reduction at different values of t_0. At short distance, the multilevel error saturates at $N_1 \approx c_2 \exp(m^\Gamma \Delta t)$. For the E^{++} channel on ensemble *gb62*, this corresponds to $\tilde{N}_1 \approx 22$ and $\tilde{N}_1 \approx 102$ for $\Delta t = 4a, 6a$, respectively. Note the largest error reduction occurs when

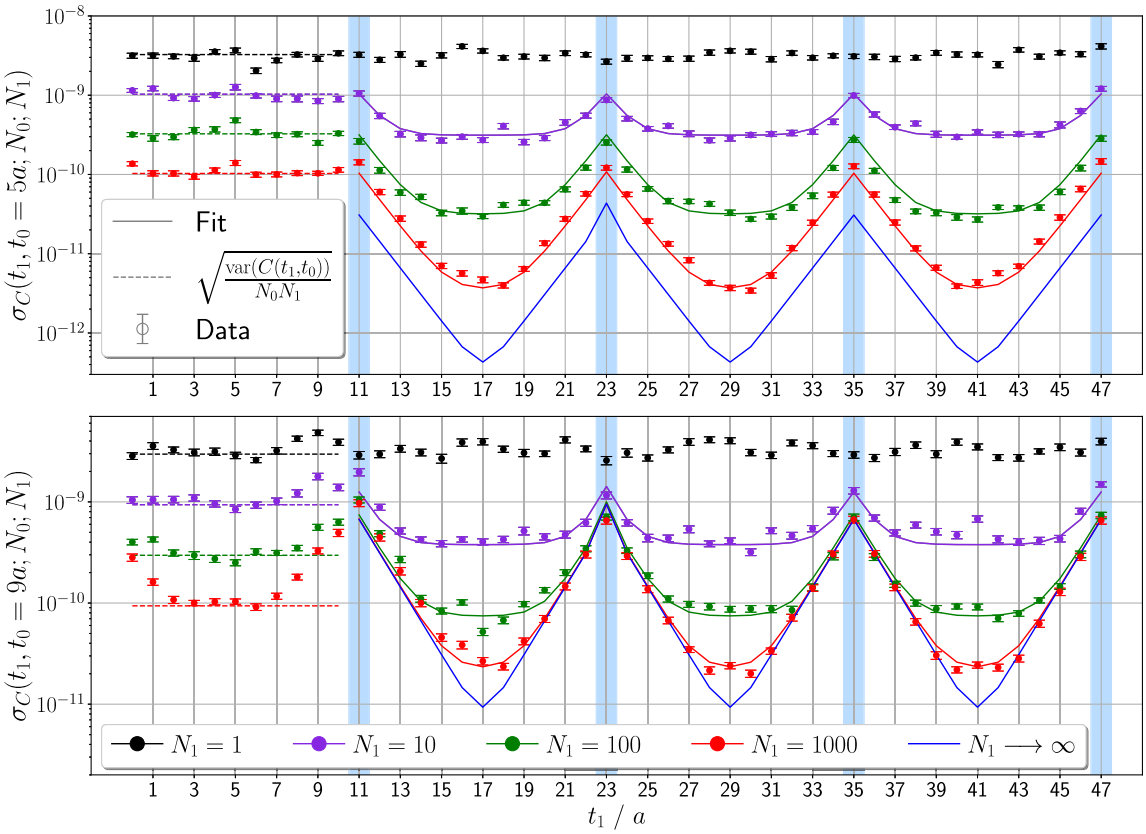

FIG. 2. Error of a single E^{++} glueball correlation function in the level-0 average at $t_0 = 5a$ (top), $9a$ (bottom), and at different values of t_1, with the ensemble *gb62* in Table I. The solid lines represent the fit formula in Eq. (13) with $c_0 = c_1 = c_2$, where we consider all the nearest boundary corrections. The dashed lines are drawn only when the operators are in the same regions and correspond to the standard scaling in Eq. (3). The light-blue shaded bands highlight the locations of the boundaries, see Fig. 1. The mass in the fit formula is set to twice the GEVP mass in the E^{++} channel ($\tilde{m} = 2m^{E^{++}} \approx 1.54/a$), see Fig. 5. We add the $N_1 \to \infty$ lines for comparison, which correspond to the square root of the third term in Eq. (13).

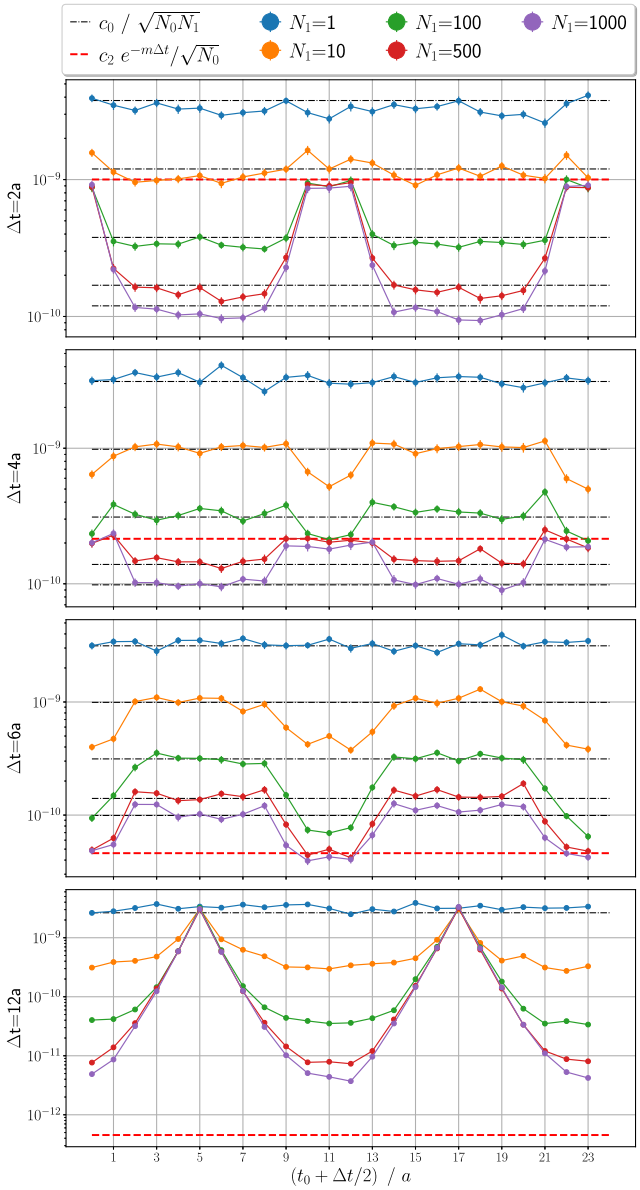

FIG. 3. Errors of one E^{++} glueball correlation function on the ensemble *gb62* at fixed values of $\Delta t = 2a$, $4a$, $6a$, $12a$, with $\Delta t = t_1 - t_0$, and with different values of N_1, t_0, and t_1. The thin black dashed lines represent the standard scaling $c_0/\sqrt{N_1}$ in Eq. (3). The red dashed line stems from the third term in Eq. (13) where $\tilde{m} = 2m^{E^{++}}$. This term is responsible for the saturation of the multilevel scaling at short distance. Notice that at $\Delta t = 2a$ and $\Delta t = 4a$, the errors are larger when the two operators are in two different regions (e.g., $t_0 + \Delta t/2 = 11a$) than when they are in the same region (e.g., $t_0 + \Delta t/2 = 3a$), even with $N_1 = 1000$. At $\Delta t = 6a$, the multilevel scaling outperforms the standard scaling. We display for clarity only half of the temporal extent of the lattice. To understand better where the operators are located, whether in the same region or not, one has to refer to Fig. 1.

the two operators are at equal distances from the boundaries ($\Delta_1 = \Delta_0 = \Delta t/2$). This is seen in Fig. 3, where the multilevel error saturates at the red dashed line for $N_1 \gg \tilde{N}_1$. As a result, it is more efficient to determine the correlation function at short distances from operator pairs in the same dynamical region rather than adopting the multilevel. The reason is that the standard error $\propto 1/\sqrt{N_1}$ is smaller than the saturated multilevel error $\propto \exp(-m^\Gamma \Delta t)$ at these short distances. Beyond $\Delta t/a = 6$, Fig. 3 shows that the multilevel scheme is more efficient than standard Monte Carlo.

C. Universal scaling toward the continuum limit

We investigate the scaling of the multilevel algorithm toward the continuum limit ($\beta = 5.8$, 6.08, and 6.2) for the glueball channels $\Gamma = A_1^{++}$, E^{++}, T_2^{++}, and A_1^{-+}. The continuum spin $J^{PC} = 0^{++}$ glueball is subduced on the lattice to the representation A_1^{++} of the cubic group of rotations, the 2^{++} glueball to the E^{++} and T_2^{++} representations and the 0^{-+} glueball to the A_1^{-+} representation. For each correlator computed at different t_1 and t_0, we consider the weighted average in Eq. (15). Figure 4 shows the noise-to-signal ratio of the weighted average glueball correlation functions in units of r_0 for a single glueball operator in all four channels.

The data shows that at small distance ($\Delta t/r_0 \lesssim 0.6$) the noise-to-signal ratio increases exponentially like $\sim \exp(m^\Gamma \Delta t)$, which is the standard scaling with traditional algorithms. The reason is at short distance, the multilevel error reduction is not large, as observed in Fig. 3, so operators located in the same region contribute more to the weighted average, because their statistical errors are smaller. It is important to mention that if one considers only operators located in two different dynamical regions, the resulting relative errors of the weighted average would be constant between $0 \le \Delta t \lesssim 1.1 r_0$ depending on the channel. This is because the multilevel error saturates at large N_1 at a value of $\sigma_C \propto \exp(-m^\Gamma \Delta t)$, which is also how the signal drops over time. At intermediate time separations ($0.6 r_0 \le \Delta t \le 1.1 r_0$), there is a change of scaling where the noise-to-signal ratio is almost constant. This region is highlighted by the shaded blue band in Fig. 4. The physical distance where the transition occurs is universal for each channel, as expected from Eq. (14) because $\exp(m^\Gamma \Delta t)$ does not depend on β. The dependence on the mass can be observed between the A_1^{++} channel and the other channels, the former contains the lightest state in the spectrum, thus requiring slightly larger time separations for the change of scaling. After this transition, the noise-to-signal ratio follows the multilevel scaling, i.e., the square root of Eq. (16), which is observed until the error of the error becomes too large. Thus, to keep the relative error constant over time at large separations, one has to set $\tilde{N}_1 \propto \exp(m^\Gamma \Delta t)$.

D. Spectrum results

To determine the glueball spectrum, we construct a basis consisting of Wilson loops with 35 different shapes,

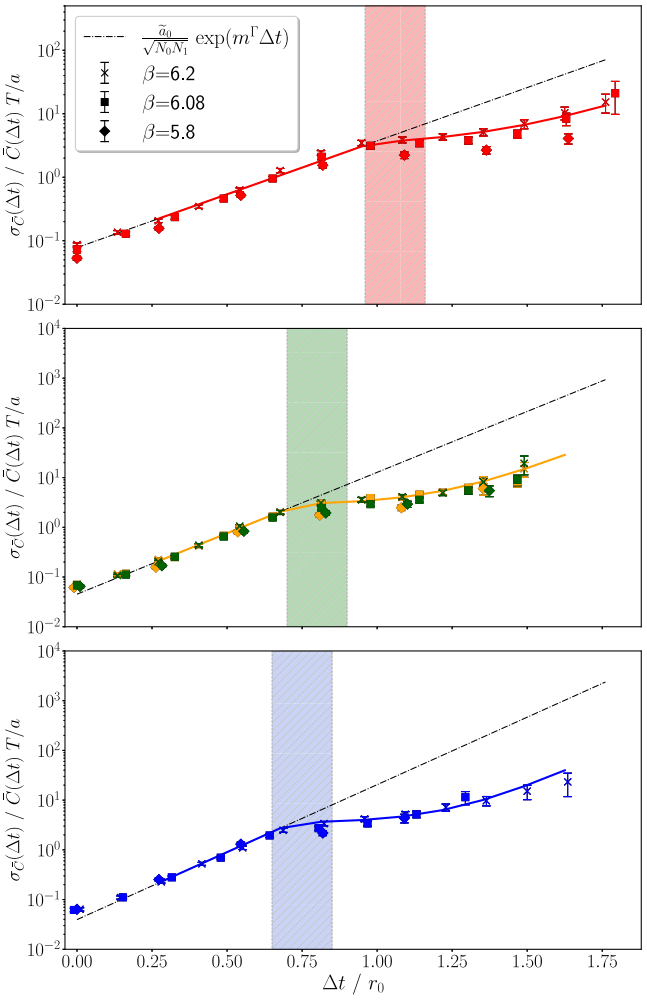

FIG. 4. The noise-to-signal ratio exhibits a universal change of scaling in units of r_0 for the channels A_1^{++} (red), E^{++} (green), T_2^{++} (orange) and A_1^{-+} (blue). The dashed lines represent the standard scaling from the Lepage-Parisi argument [35,36]. The solid lines are fits to the data at $\beta = 6.2$ using Eq. (17) at short distance (left side of bands), and Eq. (16) (right side of bands) at long distance. The bands highlight approximately where the transition between the two error scalings occurs.

as discussed in the Appendix, some of which can be projected onto the channels of interest $\Gamma = A_1^{++}$, E^{++}, T_2^{++}, and A_1^{-+} as shown in [13,58]. Each of these Wilson loops is built from links smeared with 5 different APE smearing levels [59] to construct an efficient variational basis made of up to 35×5 operators. For each operator O^Γ in this basis, we estimate the matrix of correlation functions

$$C^\Gamma_{\alpha\beta}(t_1, t_0) = \langle [\mathrm{O}^\Gamma_\alpha(t_1)][\mathrm{O}^\Gamma_\beta(t_0)]^\dagger \rangle, \qquad \alpha, \beta = 1, \ldots, N_\Gamma, \tag{19}$$

where N_Γ denotes the number of distinct operators formed from combinations of Wilson loops projected onto irrep Γ. We adopt the two-level algorithm on $N_0 = 101$ configurations with a total of $N_1 = 1000$ submeasurements to compute the matrix of correlation functions. We estimate the weighted average $\bar{C}^\Gamma_{\alpha\beta}(\Delta t)$ as discussed in the previous section, see Eq. (15). We then solve for $\Delta t > t_{\mathrm{ref}}$ the GEVP

$$\bar{C}^\Gamma(\Delta t) V^\Gamma(\Delta t, t_{\mathrm{ref}}) = \bar{C}^\Gamma(t_{\mathrm{ref}}) V^\Gamma(\Delta t, t_{\mathrm{ref}}) \Lambda^\Gamma(\Delta t, t_{\mathrm{ref}}), \tag{20}$$

where $\Lambda^\Gamma = \mathrm{diag}(\lambda_1^\Gamma(\Delta t, t_{\mathrm{ref}}), \ldots, \lambda_{N_\Gamma}^\Gamma(\Delta t, t_{\mathrm{ref}}))$ and $V^\Gamma = (v_1^\Gamma(\Delta t, t_{\mathrm{ref}}), \ldots, v_{N_\Gamma}^\Gamma(\Delta t, t_{\mathrm{ref}}))$ are the matrices of generalized eigenvalues and eigenvectors, respectively. The GEVP effective masses of ground state and further excitations m_k^Γ can be extracted from the eigenvalues as $\lambda_k^\Gamma(\Delta t, t_{\mathrm{ref}}) \propto \exp(-m_k^\Gamma(\Delta t - t_{\mathrm{ref}}))$ [60,61]. In this work, we set $t_{\mathrm{ref}} = 0a$. Some operators with different shapes might be degenerate at large enough smearing radii, as observed in Fig. 8 of [62], and thus some careful choice must be made for the optimal variational basis. Thus, we do not employ the full operator basis for each channel and, in practice, use $\mathcal{O}(10)$ operators for each glueball channel.

In Fig. 5, we present results at $\beta = 6.2$, 6.08 for the ground state of the different channels. The small irregularity at $\Delta t - t_{\mathrm{ref}} - a = 3a$ in the A_1^{-+} channel is a statistical fluctuation and is due to the loss of translational invariance of the error after combining multilevel with standard measurements. In particular, if the statistical error is slightly underestimated, it will enhance some correlators

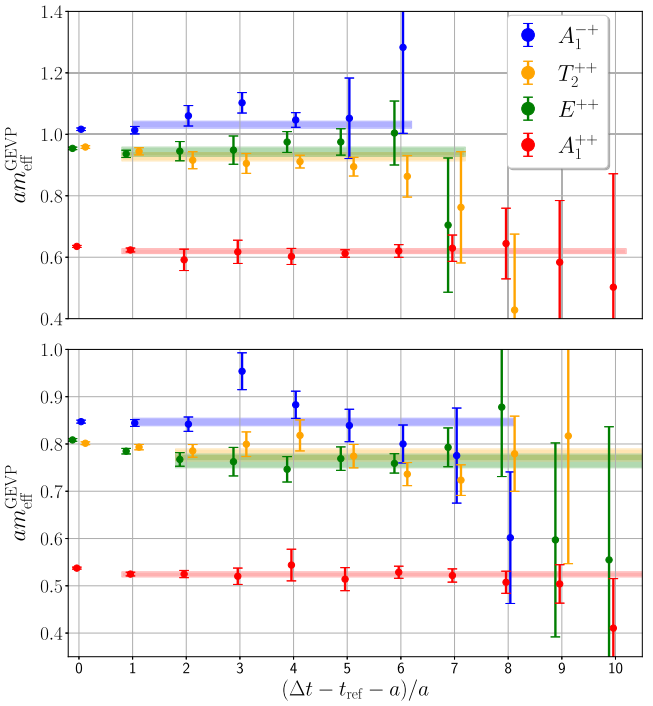

FIG. 5. Top: GEVP glueball masses at $\beta = 6.08$ for all four channels in the legend; bottom: GEVP glueball masses at $\beta = 6.2$ for all four channels.

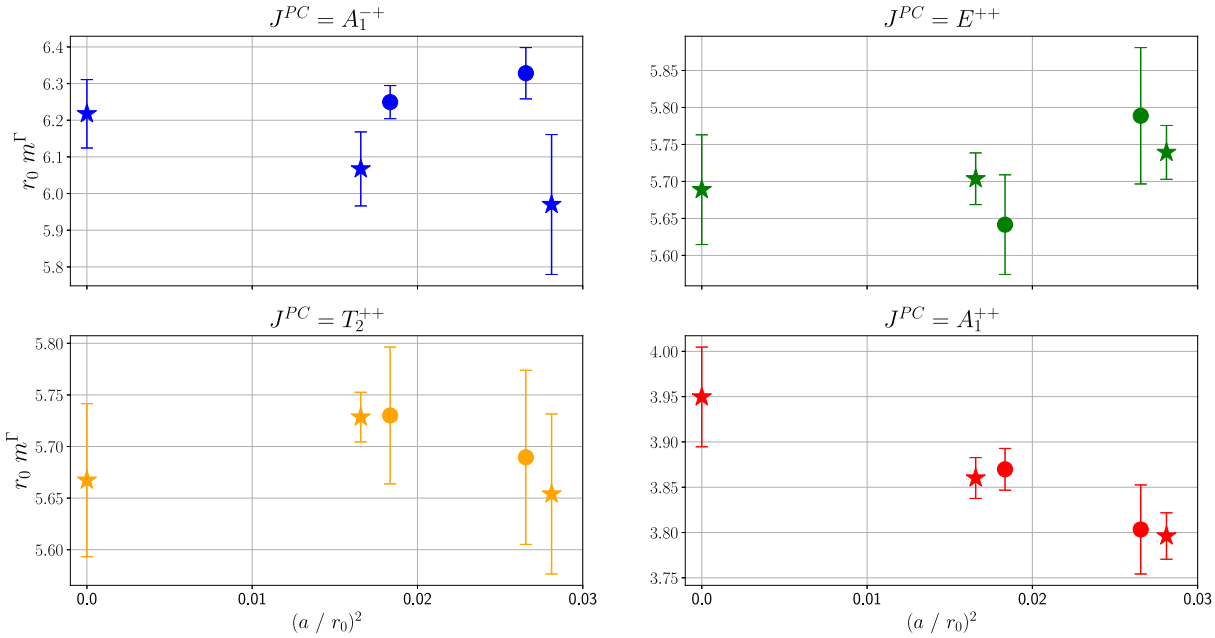

FIG. 6. Comparison between glueball masses in this work at $\beta = 6.2$, 6.08 with multilevel algorithm (circles), and state-of-the-art results (stars) at $\beta = 6.0625$, 6.235 and continuum limit results of [17], where the traditional Monte Carlo algorithm is adopted.

in the weighted average, as the weights are the inverse of the variance, see Eq. (15). A comparison with state-of-the-art results of [17] at similar β values but slightly different volumes shows that the multilevel results have smaller errors at large source-sink separations due to better scaling, as shown in Fig. 4. In particular, in Fig. 6, we show a comparison between our multilevel results at $\beta = 6.2$, 6.08 and the state-of-the-art results in [17] at $\beta = 6.235$, 6.0625. The results agree within the errors, and the statistical uncertainty is also very similar. The statistics used in the two calculations are roughly the same [$N_0 \times N_1 = \mathcal{O}(10^5)$], along with the computational cost of all the updates [$\mathcal{O}(10^6)$ MDUs], and we also adopt a large variational basis. Although the multilevel improves the noise-to-signal at large distance, cf. Fig. 4, the algorithm does not improve the final uncertainty of the glueball effective masses. Glueball masses are extracted from a fit that starts at short distance, where the multilevel does not work efficiently. This explains why the uncertainty for the final value of the glueball effective masses is roughly similar to [17], see Fig. 6. However, the multilevel signal is determined to much longer distances where the ground state dominates, which gives more confidence in the reliability of the plateau estimated at short distance. The multilevel algorithm will be necessary for investigations of glueball mixing with quark-anti-quark mesons when dynamical fermions are included as the signal drops quickly and it is challenging to understand the gluonic content of the mixed states [63]. Domain decomposition methods can be used to address the nonlocality of quark propagators arising from Wick contractions [37] and the nonlocality of the fermion determinant resulting from integrating over fermionic degrees of freedom [38], both of which hinder multilevel integration.

IV. CONCLUSIONS

We have investigated the efficiency of a two-level algorithm for determining the glueball mass spectrum in various channels toward the continuum limit. It was not *a priori* clear that the method would be efficient. As we demonstrated, the standard estimator outperforms the two-level measurements at short distances. This is primarily due to the breaking of the translational invariance by the fixed boundaries and the effect of the fixed fields on them, which limit the exploration of field space in their vicinity. With the standard method, the noise-to-signal ratio deteriorates exponentially, and the signal could be lost before the two-level estimator becomes efficient. This is complicated further because state-of-the-art analyses combine correlation functions at various source-sink separations using a sizeable variational basis with a GEVP to extract effective masses. We have demonstrated that in this setting the two-level method works. The deterioration is stopped, and the noise-to-signal ratio stays constant for a certain time interval.

The results agree very well with state-of-the-art analyses that adopt the traditional Monte Carlo. The overall statistical uncertainty is not improved; however, the GEVP masses are extracted from fits starting at short time separation, where the two-level is ineffective. Still, with the same cost as traditional Monte Carlo, the two-level algorithm can render correlation functions at long distance

with an exponentially reduced error, giving more confidence in the plateau estimate.

Depending on the channel, the two-level method is more efficient for source-sink separations above ∼0.4 fm, and we can extend the plateau region by roughly 0.25 fm using $N_1 = 1000$ submeasurements. We can reliably model the performance of the algorithm depending on the source and sink position as well as the resulting weighted averages. This allows us to understand the transition in the dominance in the average from the standard to the two-level measurements with increasing time.

The two-level Monte Carlo is an expensive method. To offset the reduced averaging in time due to the fixed regions, the number of submeasurements needs to be large, where the full power is only reached at significant source-sink separations. To ensure a reliable error analysis, boundary fields must be sampled with at least $\mathcal{O}(10^2)$ measurements. This requirement translates to a cost equivalent to taking measurements on $\mathcal{O}(10^5)$ gauge field configurations for $N_1 = 1000$.

Our study has been performed in pure gauge theory, where an operator basis can be found that allows plateau fits from very short time separations. In the presence of fermions, this is no longer possible. The large separations that can be reached with the two-level algorithm will become essential, for instance, in studies of glueball-charmonium mixing. Here standard algorithms cannot reach trustworthy plateau regions such that reliable computations need improved methods like the one investigated here.

ACKNOWLEDGMENTS

The work is supported by the German Research Foundation (DFG) research unit FOR5269 "Future methods for studying confined gluons in QCD." The authors thank all the members of the research unit for valuable discussions. L. B. is grateful to J. Frison and A. Risch for useful discussions. S. M. received funding from the European Union's Horizon 2020 research and innovation program under the Marie Skłodowska-Curie grant agreement No. 813942. This work was supported by the STRONG-2020 project, funded by the European Community Horizon 2020 research and innovation programme under grant agreement No. 824093. The authors gratefully acknowledge the scientific support and HPC resources provided by the Erlangen National High Performance Computing Center (NHR@FAU) of the Friedrich-Alexander-Universität Erlangen-Nürnberg (FAU) under the NHR project k103bf.

APPENDIX: CONSTRUCTION OF THE GLUEBALL OPERATORS

The starting point to build the glueball operators used in this work is a given loop shape, e.g., the 22 different ones presented in [13] of lengths 4, 6, and 8. A 3D Wilson loop of fixed shape starting at spatial point $\vec{x}$ and Euclidean time t is denoted as $W^s(\vec{x}, t)$, where the index s labels the shape. Elements of the cubic group can act on such a Wilson loop when it is represented as a tuple of unitary displacements equivalent under cyclic permutations thanks to the projection to zero spatial momentum [13]. The loop obtained after acting with group element g_l, $l = 0, \ldots, 23$, on $W^s(\vec{x}, t)$ is denoted as $W^s_l(\vec{x}, t)$. Considering only the l index and not any degeneracies between loops, these 24 loops form a basis which generates the regular (or permutation) representation of the cubic group, and therefore there exist linear combinations of them which transform according to any of the five irreps of this group [58,64]. A glueball operator with zero spatial momentum which transforms according to a given irrep R can be written as

$$W^{(R,k,s)}(t) = \frac{a^3}{L^3} \sum_{\vec{x}} \sum_{l=0}^{23} c_l^{R,k} \mathrm{Tr}[W^s_l(\vec{x}, t)], \qquad \text{(A1)}$$

where $k = 0, \ldots, \dim(R) - 1$ denotes the copy of irrep R which appears in the regular representation and $c_l^{R,k}$ are the projection coefficients for copy k of irrep R. These coefficients can be calculated via projection methods [58,64].

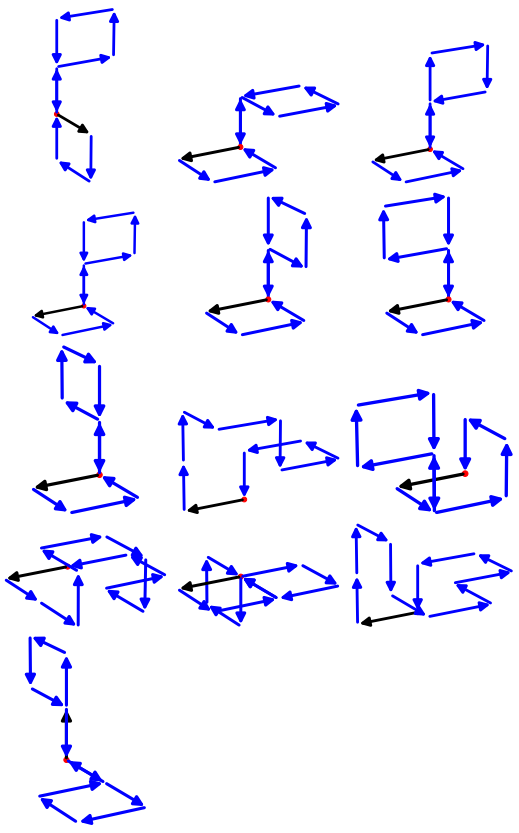

FIG. 7. Additional loop shapes used to increase the number of glueball operators.

In this work we consider only one copy per irrep so we omit the k index from now on. Parity is fixed by considering the sum ($P=+1$) or difference ($P=-1$) of each loop with its parity twin, i.e., the loop under the action of a parity transformation. The parity twin of $W_l^s(\vec{x},t)$ will be denoted as $W_l^s(\vec{x},t)^P$. Charge conjugation symmetry is fixed by taking the real ($C=+1$) or imaginary ($C=-1$) part of the trace. A glueball operator $\mathrm{O}_s^\Gamma(t)$ which transforms according to a fixed irrep $\Gamma = R^{PC}$, is given by

$$\mathrm{O}_s^{R^{\pm+}}(t) = \frac{a^3}{L^3}\sum_{\vec{x}}\sum_{l=0}^{23} c_l^R \mathrm{Re}\left\{\mathrm{Tr}\left[W_l^s(\vec{x},t) \pm W_l^s(\vec{x},t)^P\right]\right\}, \tag{A2}$$

$$\mathrm{O}_s^{R^{\pm-}}(t) = \frac{a^3}{L^3}\sum_{\vec{x}}\sum_{l=0}^{23} c_l^R \mathrm{Im}\left\{\mathrm{Tr}\left[W_l^s(\vec{x},t) \pm W_l^s(\vec{x},t)^P\right]\right\}. \tag{A3}$$

Since this construction is independent of the link smearing use, we can introduce a single index α which accounts for both the loop shape and smearing used to define a given glueball operator in the basis. In this manner, the glueball operators are denoted as $\mathrm{O}_\alpha^\Gamma(t)$ as used in Eq. (19). Once the projection coefficients are known, operators for all 20 symmetry channels can be built using the above expressions for a choice of shape; however, several of them could yield zeros. This is because not all irreps of the cubic group extended to include parity and charge conjugation are contained in the reducible representation which a given shape generates. It is the effect of taking into account the possible degeneracies between the loops under the action of the extended cubic group, which can reduce the dimension of the generated representation. For example, the plaquette cannot be used to build an operator which transforms according to any T_2^{PC}. To avoid getting these zeros, one first checks which irreps are accessible for each loop shape and only builds their corresponding operators. Tables including this irreducible content for loops of up to length 8 are given in [13]. As a final remark, only 5 out of the 22 shapes presented in [13] can be used to access the A_1^{-+} irrep. To increase the number of operators for this channel, we use 13 additional loop shapes shown in Fig. 7. Out of these, 8 have length 10 and 5 have length 12. They are chosen such that they all can be used to access the A_1^{-+} irrep as well as the A_1^{++}, E^{++}, and T_2^{++}.

[1] Harald Fritzsch and Murray Gell-Mann, Current algebra: Quarks and what else?, eConf **C720906V2**, 135 (1972).
[2] Harald Fritzsch and Peter Minkowski, Ψ resonances, gluons and the Zweig rule, Nuovo Cimento Soc. Ital. Fis. **30A**, 393 (1975).
[3] A. Chodos, R. L. Jaffe, K. Johnson, C. B. Thorn, and V. F. Weisskopf, New extended model of hadrons, Phys. Rev. D **9**, 3471 (1974).
[4] R. L. Jaffe and K. Johnson, Unconventional states of confined quarks and gluons, Phys. Lett. **60B**, 201 (1976).
[5] R. L. Jaffe, K. Johnson, and Z. Ryzak, Qualitative features of the glueball spectrum, Ann. Phys. (N.Y.) **168**, 344 (1986).
[6] Michael S. Chanowitz and Stephen R. Sharpe, Hybrids: Mixed states of quarks and gluons, Nucl. Phys. **B222**, 211 (1983); **B228**, 588(E) (1983).
[7] Nathan Isgur and Jack Paton, Flux-tube model for hadrons in QCD, Phys. Rev. D **31**, 2910 (1985).
[8] Masaharu Iwasaki, Shin-Ichi Nawa, Takayoshi Sanada, and Fujio Takagi, A flux tube model for glueballs, Phys. Rev. D **68**, 074007 (2003).
[9] J. Joseph Coyne, Paul M. Fishbane, and Sydney Meshkov, Glueballs: Their spectra, production and decay, Phys. Lett. **91B**, 259 (1980).
[10] Stephan Narison, Spectral function sum rules for gluonic currents, Z. Phys. C **26**, 209 (1984).
[11] Tao Huang, Hong-Ying Jin, and Ai-Lin Zhang, Determination of the scalar glueball mass in QCD sum rules, Phys. Rev. D **59**, 034026 (1999).
[12] Hsiang-nan Li, Dispersive analysis of glueball masses, Phys. Rev. D **104**, 114017 (2021).
[13] B. Berg and A. Billoire, Glueball spectroscopy in four-dimensional SU(3) lattice gauge theory. 1, Nucl. Phys. **B221**, 109 (1983).
[14] G. S. Bali, K. Schilling, A. Hulsebos, A. C. Irving, Christopher Michael, and P. W. Stephenson, A comprehensive lattice study of SU(3) glueballs, Phys. Lett. B **309**, 378 (1993).
[15] Colin J. Morningstar and Mike J. Peardon, The glueball spectrum from an anisotropic lattice study, Phys. Rev. D **60**, 034509 (1999).
[16] Y. Chen *et al.*, Glueball spectrum and matrix elements on anisotropic lattices, Phys. Rev. D **73**, 014516 (2006).
[17] Andreas Athenodorou and Michael Teper, The glueball spectrum of SU(3) gauge theory in $3+1$ dimensions, J. High Energy Phys. 11 (2020) 172.
[18] W. Erni, I. Keshelashvili, B. Krusche *et al.*, Physics performance report for PANDA: Strong interaction studies with antiprotons, arXiv:0903.3905.
[19] Alexey A. Petrov, Glueball-meson molecules, Phys. Lett. B **843**, 138030 (2023).
[20] Eberhard Klempt and Andrey V. Sarantsev, Singlet-octet-glueball mixing of scalar mesons, Phys. Lett. B **826**, 136906 (2022).
[21] Claude Amsler and Frank E. Close, Is $f_0(1500)$ a scalar glueball?, Phys. Rev. D **53**, 295 (1996).
[22] John F. Donoghue, K. Johnson, and Bing An Li, Low mass glueballs in the meson spectrum, Phys. Lett. **99B**, 416 (1981).

[23] Simon Kiesewetter and Vicente Vento, $\eta - \eta' -$ glueball mixing, Phys. Rev. D **82**, 034003 (2010).

[24] V. Crede and C. A. Meyer, The experimental status of glueballs, Prog. Part. Nucl. Phys. **63**, 74 (2009).

[25] M. Ablikim *et al.*, Determination of spin-parity quantum numbers of $X(2370)$ as 0^{-+} from $J/\psi \to \gamma K_S^0 K_S^0 \eta'$, Phys. Rev. Lett. **132**, 181901 (2024).

[26] E. Gregory, A. Irving, B. Lucini, C. McNeile, A. Rago, C. Richards, and E. Rinaldi, Towards the glueball spectrum from unquenched lattice QCD, J. High Energy Phys. 10 (2012) 170.

[27] A. Hart and M. Teper, On the glueball spectrum in O(a) improved lattice QCD, Phys. Rev. D **65**, 034502 (2002).

[28] Gunnar S. Bali, Bram Bolder, Norbert Eicker, Thomas Lippert, Boris Orth, Peer Ueberholz, Klaus Schilling, and Thorsten Struckmann, Static potentials and glueball masses from QCD simulations with Wilson sea quarks, Phys. Rev. D **62**, 054503 (2000).

[29] A. Hart, C. McNeile, C. Michael, and J. Pickavance, Lattice study of the masses of singlet 0^{++} mesons, Phys. Rev. D **74**, 114504 (2006).

[30] Long-Cheng Gui, Ying Chen, Gang Li, Chuan Liu, Yu-Bin Liu, Jian-Ping Ma, Yi-Bo Yang, and Jian-Bo Zhang, Scalar glueball in radiative J/ψ decay on the lattice, Phys. Rev. Lett. **110**, 021601 (2013).

[31] Yi-Bo Yang, Long-Cheng Gui, Ying Chen, Chuan Liu, Yu-Bin Liu, Jian-Ping Ma, and Jian-Bo Zhang, Lattice study of radiative J/ψ decay to a tensor glueball, Phys. Rev. Lett. **111**, 091601 (2013).

[32] Long-Cheng Gui, Jia-Mei Dong, Ying Chen, and Yi-Bo Yang, Study of the pseudoscalar glueball in J/ψ radiative decays, Phys. Rev. D **100**, 054511 (2019).

[33] M. Luscher, Volume dependence of the energy spectrum in massive quantum field theories. 2. Scattering states, Commun. Math. Phys. **105**, 153 (1986).

[34] Raul A. Briceno and Zohreh Davoudi, Three-particle scattering amplitudes from a finite volume formalism, Phys. Rev. D **87**, 094507 (2013).

[35] G. Parisi, The strategy for computing the hadronic mass spectrum, Phys. Rep. **103**, 203 (1984).

[36] G. Peter Lepage, The analysis of algorithms for lattice field theory, in *Theoretical Advanced Study Institute in Elementary Particle Physics* (1989), https://cds.cern.ch/record/206049.

[37] Marco Cè, Leonardo Giusti, and Stefan Schaefer, Domain decomposition, multi-level integration and exponential noise reduction in lattice QCD, Phys. Rev. D **93**, 094507 (2016).

[38] Marco Cè, Leonardo Giusti, and Stefan Schaefer, A local factorization of the fermion determinant in lattice QCD, Phys. Rev. D **95**, 034503 (2017).

[39] Leonardo Giusti, Marco Cè, and Stefan Schaefer, Multiboson block factorization of fermions, EPJ Web Conf. **175**, 01003 (2018).

[40] Marco Cè, Leonardo Giusti, and Stefan Schaefer, Local multiboson factorization of the quark determinant, EPJ Web Conf. **175**, 11005 (2018).

[41] Marco Cè, Locality and multi-level sampling with fermions, Eur. Phys. J. Plus **134**, 299 (2019).

[42] G. Parisi, R. Petronzio, and F. Rapuano, A measurement of the string tension near the continuum limit, Phys. Lett. **128B**, 418 (1983).

[43] Martin Lüscher and Peter Weisz, Locality and exponential error reduction in numerical lattice gauge theory, J. High Energy Phys. 09 (2001) 010.

[44] Harvey B. Meyer, Locality and statistical error reduction on correlation functions, J. High Energy Phys. 01 (2003) 048.

[45] Harvey B. Meyer, The Yang-Mills spectrum from a two level algorithm, J. High Energy Phys. 01 (2004) 030.

[46] M. Hasenbusch and S. Necco, SU(3) lattice gauge theory with a mixed fundamental and adjoint plaquette action: Lattice artifacts, J. High Energy Phys. 08 (2004) 005.

[47] Pushan Majumdar, Nilmani Mathur, and Sourav Mondal, Noise reduction algorithm for Glueball correlators, Phys. Lett. B **736**, 415 (2014).

[48] Lorenzo Barca, Francesco Knechtli, Michael Peardon, Stefan Schaefer, and Juan Andrés Urrea-Niño, Performance of two-level sampling for the glueball spectrum in pure gauge theory, Proc. Sci. LATTICE2023 (2023) 030.

[49] C. Michael and I. Teasdale, Extracting glueball masses from lattice QCD, Nucl. Phys. **B215**, 433 (1983).

[50] Benoit Blossier, Michele Della Morte, Georg von Hippel, Tereza Mendes, and Rainer Sommer, On the generalized eigenvalue method for energies and matrix elements in lattice field theory, J. High Energy Phys. 04 (2009) 094.

[51] John Bulava, Michael Donnellan, and Rainer Sommer, On the computation of hadron-to-hadron transition matrix elements in lattice QCD, J. High Energy Phys. 01 (2012) 140.

[52] Anne Mykkanen, The static quark potential from a multi-level algorithm for the improved gauge action, J. High Energy Phys. 12 (2012) 069.

[53] Miguel García Vera and Stefan Schaefer, Multilevel algorithm for flow observables in gauge theories, Phys. Rev. D **93**, 074502 (2016).

[54] Ben Kitching-Morley and Andreas Jüttner, A numerical and theoretical study of multilevel performance for two-point correlator calculations, Proc. Sci. LATTICE2021 (**2022**) 133.

[55] Martin Lüscher *et al.*, OpenQCD, https://luscher.web.cern.ch/luscher/openQCD/.

[56] Martin Luscher and Stefan Schaefer, Lattice QCD with open boundary conditions and twisted-mass reweighting, Comput. Phys. Commun. **184**, 519 (2013).

[57] Silvia Necco and Rainer Sommer, The $N_f = 0$ heavy quark potential from short to intermediate distances, Nucl. Phys. **B622**, 328 (2002).

[58] Howard Georgi, *Lie Algebras in Particle Physics: From Isospin to Unified Theories* (Perseus, Cambridge, 2018).

[59] M. Falcioni, M. L. Paciello, G. Parisi, and B. Taglienti, Again on SU(3) glueball mass, Nucl. Phys. **B251**, 624 (1985).

[60] Martin Lüscher and Ulli Wolff, How to calculate the elastic scattering matrix in two-dimensional quantum field theories by numerical simulation, Nucl. Phys. **B339**, 222 (1990).

[61] Benoit Blossier, Michele Della Morte, Georg von Hippel, Tereza Mendes, and Rainer Sommer, On the generalized eigenvalue method for energies and matrix elements in lattice field theory, J. High Energy Phys. 04 (2009) 094.
[62] Keita Sakai and Shoichi Sasaki, Glueball spectroscopy in lattice QCD using gradient flow, Phys. Rev. D **107**, 034510 (2023).
[63] Juan Andrés Urrea-Niño, Jacob Finkenrath, Roman Höllwieser, Francesco Knechtli, Tomasz Korzec, and Michael J. Peardon, Charmonium spectroscopy with optimal distillation profiles, Proc. Sci. LATTICE2023 (**2024**) 061.
[64] P. R. Bunker and P. Jensen, *Molecular Symmetry and Spectroscopy*, 2nd ed. (NRC Press, Ottawa, ON, Canada, 1998).